Journal of Applied Fluid Mechanics, Vol. 9, No. 3, pp. 1135-1146, 2016.
Available online at www.jafmonline.net, ISSN 1735-3572, EISSN 1735-3645.
DOI: 10.18869/acadpub.jafm.68.228.24295

A Novel Multidimensional Characteristic Modeling of Incompressible Convective Heat Transfer

S. E. Razavi[1] and T. Adibi[2†]

[1] *School of Mechanical Engineering, University of Tabriz, Tabriz, Azarbaijanshargi, Iran*
[2] *School of Engineering, University of Bonab, Bonab, Azarbaijansharghi, Iran*

†*Corresponding Author Email: Tohidadibi@gmail.com, Tohidadibi@tabrizu.ac.ir*

(Received December 5, 2014; accepted April 29, 2015)

ABSTRACT

A characteristic-based approach is developed for thermo-flow with finite volume methodology (FVM) in which multidimensional characteristic (MC) scheme is applied for convective fluxes. Artificial compressibility (AC) is used, and as a result governing equations take the hyperbolic nature. To obtain compatibility equations and pseudo characteristics, energy equation is taken into account in the MC scheme. With MC scheme for convective fluxes, no artificial viscosity is required even at high Reynolds numbers. As benchmarks, forced convection between parallel plates and forced and mixed convection in a cavity are examined for a wide range of Reynolds, Grashof and Prandtl numbers. First-order MC and second-order averaging schemes are used for simulate them. Results show the better performance of MC scheme in force convection as well as mixed convection. Results confirm the robustness of MC scheme in terms of accuracy and convergence, and are in good agreement with the standard benchmark solutions in the literature.

Keywords: Multidimensional characteristics; Navier-stokes equations; Artificial compressibility; Mixed convection; Finite volume method.

NOMENCLATURE

cp	specific heat capacity
Ec	Eckert number
g	gravitational acceleration
Gr	Grashof number
k	thermal conductivity
Nu	local Nusselt number
p	pressure
Pr	Prandtl number
Re	Reynolds number
T	temperature
t	time
u, v	x–y velocity components
x, y	Cartesian coordinates
β	artificial compressibility coefficient
βe	thermal expansion coefficient
x	coefficient of viscosity
μ	kinematic viscosity
υ	density of the fluid
ρ	

Subscripts

ref	reference

1. INTRODUCTION

Many numerical approaches for incompressible flows are mainly based on the pressure corrections. Artificial compressibility (AC) of Chorin (Chorin 1997) is an alternative among the others. Where, by the aid of pseudo-time derivative, the continuity and momentum equations are coupled. Consequently, the hyperbolized governing equations admit the compressible flow schemes. Flux modeling in FVM has been a challenging issue up to now. In the meantime, the flux averaging has served in a vast part of applications, but its main defect (poor stability) is still remaining. Characteristic-based schemes have been developed to overcome this problem. Tamamidis *et al* (Tamamidis, Zhang *et al*. 1996) compared the pressure-based and artificial compressibility methods for calculating laminar steady, incompressible viscous flows. The most attractive feature of the AC is its faster convergence. The AC requires one adjustable parameter for convergence control. While the pressure based method typically requires two

under relaxation factors. The characteristic based (CB) method was extended for two-dimensional modified incompressible flows by Drikakis *et al*.(Drikakis, Govatsos *et al*. 1994). They applied CB method for convective fluxes within the FV framework. The normal component of convective fluxes was used as well to 3D flow. Shakir *et al*. (Shakir, Mohammed *et al*. 2011) discretized the governing equations by upwind differencing, and used by SIMPLE method on staggered grid. Tmartnhad (Tmartnhad, El Alami *et al*. 2008) carried out a numerical study of mixed convection in a trapezoidal cavity. The Navier–Stokes equations were solved using SIMPLEC. Ohwada *et al*. (Ohwada, Asinari *et al*. 2011) compared the AC and the lattice Boltzmann methods(LBM). The robustness of the AC was enhanced by introducing a new dissipation term. Their results confirmed that the fortified AC is more robust as well as accurate than the LBM. Gasemi and Razavi (Ghasemi and Razavi 2010) developed thermal finite volume LBM. The upwind biasing factors based on pressure and temperature, were used as flux corrector in the thermo-hydrodynamic lattice Boltzmann equations. Haeri and Shrimpton (Haeri and Shrimpton 2013) used an implicit fictitious domain method where the entire domain was assumed to be incompressible. They used the SIMPLE algorithm with a collocated grid for free and forced convections. Srinivasa and Eswara (Srinivasa and Eswara 2013) simulated unsteady free convection over an isothermal truncated cone with variable viscosity and Prandtl number. An implicit finite-difference scheme along with quasilinearization was used for solving coupled thermo-flow equations. Raji *et al*. (Raji, Hasnaoui *et al*. 2012) utilized SIMPLER for free convection in a square cavity. The convective fluxes were evaluated by hybrid scheme in which the central differences are replaced by first-order upwind scheme. Selimefendigil and Öztop (Selimefendigil and Öztop 2014) performed numerical investigation of pulsating mixed convection in a multiply vented cavity for a range of Reynolds, Grashof, and Strouhal numbers. The convective fluxes in momentum and energy equations were solved by QUICK, and SIMPLE was used for velocity-pressure coupling. Sivasankaran *et al*. (Sivasankaran, Sivakumar *et al*. 2013) carried out numerical analysis on mixed convection in an inclined square cavity with different sizes and heater locations. The first-order upwind and second-order central schemes were used for the convective and diffusion fluxes, respectively. Billah *et al*. (Billah, Rahman *et al*. 2011) analyzed mixed convection heat transfer in a lid-driven cavity and a heated circular hollow cylinder positioned at the center of the cavity. A Galerkin weighted residual finite element method was adopted to solve the governing equations. Santos *et al*. (dos Santos, Piccoli *et al*. 2011) performed large eddy simulation of mixed convection in transient, laminar, and turbulent flows in cavities. The Smagorinsky model was employed for the sub-grid treatment. The simulations were based on the finite elements. Rehena Nasrin and Abdul Alim (Rehena Nasrin and Alim 2014) simulated forced convection in solar pipes. They solved governing partial equations using the finite element simulation with galerkin's weighted residual techniques. Ahmad Reza Rahmati

et al (Ahmad Reza Rahmati, M. Ashrafizaadeh *et al*. 2014) simulated lid-driven cavity flow. They used the Multi-Relaxation-Time Lattice Boltzmann (MRT-LB) model for large-eddy simulation (LES) of turbulent thermally driven flows on non-uniform grids. The simulation results showed that lattice Boltzmann method is capable to simulate turbulent convection flow problems at high Rayleigh numbers.

Here, the MC method is developed for incompressible flow with heat transfer and mathematical structures of 2D characteristics for incompressible termo-flow equations in conjunction with AC are derived. By the aid of derived compatibility relations, a scheme for incompressible flow with heat transfer was presented. The new scheme is applied for flow between parallel plates and lid-driven cavity flow for a wide range of Reynolds, Grashof, and Prandtl numbers, in order to show its ability.

2. GOVERNING EQUATIONS

The governing equations for incompressible thermo-flow can be expressed as

$$\frac{\partial}{\partial t}\iint \mathbf{Q}dA + \oint\left((\mathbf{F}-\mathbf{R})dy - (\mathbf{G}-\mathbf{S})dx\right) = \iint \mathbf{H}dA,$$

$$\mathbf{Q}=\begin{bmatrix} p \\ u \\ v \\ T \end{bmatrix},\quad \mathbf{F}=\begin{bmatrix} \beta u \\ p+u^2 \\ uv \\ (T-Ec\ p)u \end{bmatrix},\quad \mathbf{G}=\begin{bmatrix} \beta v \\ uv \\ p+v^2 \\ (T-Ec\ p)v \end{bmatrix},$$

$$\mathbf{R}=\frac{1}{\mathrm{Re}}\begin{bmatrix} 0 \\ \frac{\partial u}{\partial x} \\ \frac{\partial v}{\partial x} \\ \frac{1}{\mathrm{Pr}}\frac{\partial T}{\partial x} \end{bmatrix},\ \mathbf{S}=\frac{1}{\mathrm{Re}}\begin{bmatrix} 0 \\ \frac{\partial u}{\partial y} \\ \frac{\partial v}{\partial y} \\ \frac{1}{\mathrm{Pr}}\frac{\partial T}{\partial y} \end{bmatrix},\quad \mathbf{H}=\begin{bmatrix} 0 \\ 0 \\ \frac{Gr}{\mathrm{Re}^2}T \\ \frac{Ec}{\mathrm{Re}}\Phi \end{bmatrix},$$

$$\Phi=\left(\frac{\partial u}{\partial y}+\frac{\partial v}{\partial x}\right)^2+2\left(\left(\frac{\partial u}{\partial x}\right)^2+\left(\frac{\partial v}{\partial y}\right)^2\right),$$

$$\mathrm{Re}=\frac{\rho_{ref}\,u_{ref}\,L_{ref}}{\mu},\qquad \mathrm{Pr}=\frac{c_P\,\mu}{k},$$

$$Ec=\frac{u_{ref}^2}{c_P\left(T_{ref\,2}-T_{ref\,1}\right)},$$

$$Gr=\frac{\beta_{ex}\,g\left(T_{ref\,2}-T_{ref\,1}\right)L_{ref}^3}{\upsilon^2}.$$

(1)

It is noted that the above system has been modified by AC, and nondimensionalized by the following

parameters. For facility the " *" has been omitted.

$$u^* = \frac{u}{U_{ref}}, v^* = \frac{v}{U_{ref}}, x^* = \frac{x}{L_{ref}}, y^* = \frac{y}{L_{ref}},$$
$$p^* = \frac{p + \rho g y - p_\infty}{\rho_{ref} U_{ref}^2}, t^* = \frac{t U_{ref}}{L_{ref}},$$

$$T^* = \frac{T - T_{ref\,1}}{T_{ref\,2} - T_{ref\,1}}. \quad (2)$$

3. MC SCHEME DERIVATION

The time axis is considered to be normal to the physical plane. Therefore, the pseudo-velocity vector is defined as $\mathbf{V} = u\,\mathbf{i} + v\,\mathbf{j} + \mathbf{k}$, where k is the unit vector along the time axis. The path traced out by a fluid particle in "x, y, t" space is named the pseudo-pathline, The projection of the pseudo-pathline on the physical plane is the particle pathline. To determine the characteristics and compatibility equations, governing equations are multiplied by the unknown parameters, σ_1 to σ_4, and summed. Thus, one has

$$\sigma_1 * Con. + \sigma_2 * x_{Mom.} + \sigma_3 * y_{Mom.} + \sigma_4 * enrg. = 0$$

$$\sigma_1 \frac{\partial p}{\partial t} + \sigma_2 \frac{\partial p}{\partial x} + \sigma_3 \frac{\partial p}{\partial y} + \sigma_2 \frac{\partial u}{\partial t} + (\sigma_1 \beta + u\sigma_2)\frac{\partial u}{\partial x} + (v\sigma_2)\frac{\partial u}{\partial y} + \sigma_3 \frac{\partial v}{\partial t} + (u\sigma_3)\frac{\partial v}{\partial x} + (\sigma_1 \beta + v\sigma_3)\frac{\partial v}{\partial y} + \sigma_4\left(\frac{\partial T}{\partial t} + u\frac{\partial T}{\partial x} + v\frac{\partial T}{\partial y}\right) = 0,$$

where $\sigma_1, \sigma_2, \sigma_3$, and σ_4 are unknown constants. The vectors with components which are the coefficients of the partial derivatives in Eq. (3) are defined as following

$$\begin{aligned} \mathbf{W_1} &= \sigma_2 \mathbf{i} + \sigma_3 \mathbf{j} + \sigma_1 \mathbf{k}, \\ \mathbf{W_2} &= (\sigma_1 \beta + u\sigma_2)\mathbf{i} + (v\sigma_2)\mathbf{j} + \sigma_2 \mathbf{k}, \\ \mathbf{W_3} &= u\sigma_3 \mathbf{i} + (\sigma_1 \beta + v\sigma_3)\mathbf{j} + \sigma_3 \mathbf{k}, \\ \mathbf{W_4} &= u\sigma_4 \mathbf{i} + v\sigma_4 \mathbf{j} + \sigma_4 \mathbf{k}. \end{aligned} \quad (4)$$

Therefore, Eq. (3) may be transformed to read

$$d_{w\,1}p + d_{w\,2}u + d_{w\,3}v + d_{w\,4}T = 0, \quad (5)$$

where $d_{w\,1}p$ defines the derivative of "p" along "W_1", etc. Hence Eq. (5) is being the compatibility equation of 2D incompressible thermo-flow. Now, the normal vector of characteristic surface is defined as

$$\mathbf{N} = n_x \mathbf{i} + n_y \mathbf{j} + n_t \mathbf{k}, \quad (6)$$

where $n_x^2 + n_y^2 = 1$. Unknown constants must be chosen such that the W vectors to lie on the same surface that is called characteristic surface. The relation to satisfy this issue reads

$$\mathbf{N}.\,\mathbf{W}_j = 0, \quad j = 1, 2, 3, 4. \quad (7)$$

Eq. (7) displays four equations with four unknowns. To have nontrivial solution i.e. (any σ is not zero) the determinant of coefficient matrix must be zero.

$$\begin{vmatrix} n_t & n_x & n_y & 0 \\ \beta n_x & un_x + vn_y + n_t & 0 & 0 \\ \beta n_y & 0 & un_x + vn_y + n_t & 0 \\ 0 & 0 & 0 & un_x + vn_y + n_t \end{vmatrix} = 0, \quad (8)$$

which leads to

$$(un_x + vn_y + n_t)^2 \left(n_t(un_x + vn_y + n_t) - \beta\left(n_x^2 + n_y^2\right)\right) = 0. \quad (9)$$

It should be noted that Eq. (9) has four real roots which are displayed as

$$\begin{aligned} n_t &= -un_x - vn_y \quad \text{(double root)}, \\ n_t &= \frac{1}{2}(-un_x - vn_y \pm \sqrt{(un_x + vn_y)^2 + 4\beta}). \end{aligned} \quad (10)$$

The tangent vector to characteristic line is expressed as $\mathbf{L} = dx\,\mathbf{i} + dy\,\mathbf{j} + dt\,\mathbf{k}$. Which is perpendicular to normal vector (**N**) then $\mathbf{N}.\,\mathbf{L} = 0$. By substitution of Eq. (10) in the last relation, the following equations are obtained.

$$dx\,n_x + dy\,n_y + dt\left(-un_x - vn_y\right) = 0 \quad \text{(twice)},$$

$$\rightarrow \quad \frac{dx}{dt} = u, \ \frac{dy}{dt} = v,$$

$$dx\,n_x + dy\,n_y + dt\left(\frac{-un_x - vn_y \pm \sqrt{(-un_x - vn_y)^2 + 4\beta}}{2}\right) = 0,$$

hence

$$\begin{aligned} \frac{dx}{dt} &= \frac{-n_x}{2}\left(-un_x - vn_y \pm \sqrt{(un_x + vn_y)^2 + 4\beta}\right), \\ \frac{dy}{dt} &= \frac{-n_y}{2}\left(-un_x - vn_y \pm \sqrt{(un_x + vn_y)^2 + 4\beta}\right). \end{aligned} \quad (11)$$

The first equation shows pseudo-pathline, and the second one demonstrates the characteristic surfaces. These are shown in Fig. 1.

The cross-section of characteristic surfaces with the physical plane is obtained by numerical solution. For this purpose, one needs to define $n_x = \cos(\theta)$, $n_y = \sin(\theta)$. Then the numerical solution of Eq. (11) becomes

$$x = x^* + \frac{\cos(\theta)}{2}\left(-u\cos(\theta) - v\sin(\theta) \pm \sqrt{(u\cos(\theta) + v\sin(\theta))^2 + 4\beta}\right)\Delta t,$$

$$y = y^* + \frac{\sin(\theta)}{2}$$

$$\left(-u\cos(\theta) - v\sin(\theta) \pm \sqrt{(u\cos(\theta) + v\sin(\theta))^2 + 4\beta}\right)\Delta t,$$

where "x^*" and "y^*" denote the cone vertex as shown in Fig. 1, which are obtained for ($0 < \theta < 2\pi$). The cone cross-section is displayed in Fig. 2 for different values of "β". In the compressible flow, this cross-section is a circle. As $\sqrt{\beta}$ tends to larger values the cross-section could become circle. In this case, $\sqrt{\beta}$ is the pseudo speed of sound in the incompressible flow.

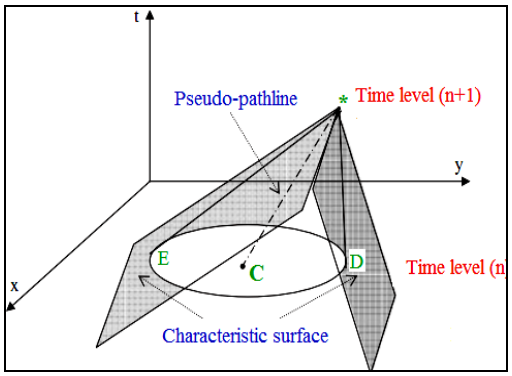

Fig. 1. Characteristic surfaces and pseudo path line.

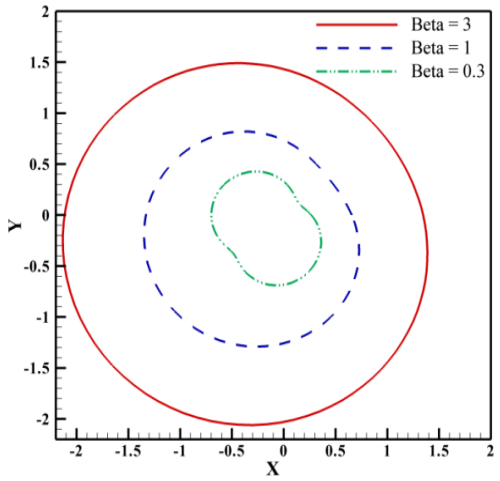

Fig. 2. Cross-section of pseudo mach cone reforming in physical plane.

The first "n_t" is substituted by its value in Eq. (7) then

$$\sigma_1 = 0, \qquad \sigma_2 = -\frac{n_y}{n_x}\sigma_3, \qquad \sigma_3, \sigma_4 = arbitrary. \tag{13}$$

By choosing $\sigma_3 = 0,\ \sigma_4 = 1$, the first compatibility equation is obtained as

$$\frac{\partial T}{\partial t} + u\frac{\partial T}{\partial x} + v\frac{\partial T}{\partial y} = 0. \tag{14}$$

Above equation on its corresponding characteristic line which is demonstrated by Eq. (11), is changed into an ordinary differential equation (ODE) as $\frac{dT}{dt} = 0$. Other compatibility equations have been obtained by the same procedure and are shown as

For second compatibility equations one sets

$$\sigma_1 = 0, \qquad \sigma_2 = -\frac{n_y}{n_x}, \qquad \sigma_3 = 1, \quad \sigma_4 = 0,$$

$$-n_y\frac{\partial p}{\partial x} + n_x\frac{\partial p}{\partial y} - n_y\frac{du}{dt} + n_x\frac{dv}{dt} = 0 \quad .$$

Similarity for third and fourth compatibility equations one assigns

$$\sigma_1 = 1, \quad \sigma_2 = -a, \quad \sigma_3 = -b, \quad \sigma_4 = 0$$

$$\frac{dp}{dt} - a\frac{\partial u}{\partial t} + (\beta - au)\frac{\partial u}{\partial x} - (av)\frac{\partial u}{\partial y}$$
$$-b\frac{\partial v}{\partial t} - (bu)\frac{\partial v}{\partial x} + (\beta - bv)\frac{\partial v}{\partial y} = 0$$

where

$$a = \frac{n_x}{2}(-un_x - vn_y \pm \sqrt{(un_x + vn_y)^2 + 4\beta}),$$

$$b = \frac{n_y}{2}(-un_x - vn_y \pm \sqrt{(un_x + vn_y)^2 + 4\beta})$$

(15)

Unlike the first compatibility equation, the others do not recast into ODE. Therefore, one has to use 1D assumption to obtain the other compatibility equations. For this purpose, previous procedure has been carried out by considering 1D flow. Results are obtained as

$$\begin{vmatrix} n_t & n_x \\ \beta n_x & un_x + vn_y + n_t \end{vmatrix} = 0 \quad \rightarrow$$

$$n_t(un_x + vn_y + n_t) - \beta n_x^2 = 0 \quad \rightarrow$$

$$n_t = \frac{1}{2}(-u \pm \sqrt{u^2 + 4\beta})$$

$$\frac{dp}{dt} - \frac{1}{2}(-u \pm \sqrt{u^2 + 4\beta})\frac{du}{dt} = 0$$

(compatibility equations)

$$\frac{dx}{dt} = -\frac{1}{2}(-u \pm \sqrt{u^2 + 4\beta}) \quad \text{(characteristic lines)}$$

(16)

4. FLUX COMPUTATION IN FVM

The governing equations in discretized form read

$$A_{ij}\frac{\partial \mathbf{Q}_{ijk}}{\partial t} =$$

$$\left[\sum_{m=1}^{4}\left(\left(\mathbf{F}_{ijk} - \mathbf{R}_{ijk}\right)\Delta y - \left(\mathbf{G}_{ijk} - \mathbf{S}_{ijk}\right)\Delta x\right)_m - A_{ij}\mathbf{H}_{ijk}\right],$$

(17)

Two schemes are used for calculation of convective fluxes, the averaging and MC. In MC scheme

convective fluxes are calculated along the characteristics. After discretization of compatibility equations along their corresponding characteristic line one has

$$(p^*)^{n+1}-(p_D)^n+\frac{1}{2}(u-\sqrt{u^2+4\beta}\,)$$
$$((u^*)^{n+1}-(u_D)^n)=0$$
$$x_D=x^*-(u-\sqrt{u^2+4\beta})\frac{\Delta t}{2},$$

$$(p^*)^{n+1}-(p_E)^n+\frac{1}{2}(u+\sqrt{u^2+4\beta})$$
$$((u^*)^{n+1}-(u_E)^n)=0$$
$$x_E=x^*-(u+\sqrt{u^2+4\beta})\frac{\Delta t}{2},$$

$$(T^*)^{n+1}=(T_C)^n\ ,$$

$$x_C=x^*-u\Delta t\ ,\quad y_C=y^*-v\Delta t.$$

(18)

In MC, convective fluxes are calculated at time level (n+1); as a result this is semi implicit. By simultaneous solution of Eqs. (17), $p^*, u^*, and\ T^*$ are obtained as

$$(u^*)^{n+1}=\frac{1}{\sqrt{u^2+4\beta}}((p_E)^n-(p_D)^n+$$
$$\frac{1}{2}(u+\sqrt{u^2+4\beta})(u_E)^n-\frac{1}{2}(u-\sqrt{u^2+4\beta})(u_D)^n)$$
$$(p^*)^{n+1}=(p_E)^n-\frac{1}{2}(u+\sqrt{u^2+4\beta})((u^*)^{n+1}-(u_E)^n),$$
$$(T^*)^{n+1}=(T_C)^n.$$

(19)

Point "C" is on the same pseudo line with (*) point as displayed in Fig. 1. The projection of these points on the physical plane is shown in Fig. 3. Points "D" and "E" are on the same characteristic lines with (*) point. These points are displayed in Fig. 4.

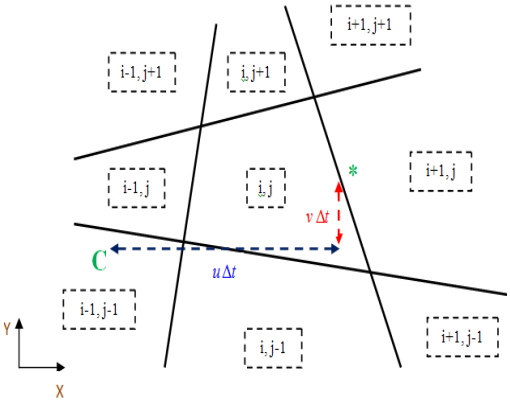

Fig. 3. Pattern for calculation of convective fluxes for energy equation.

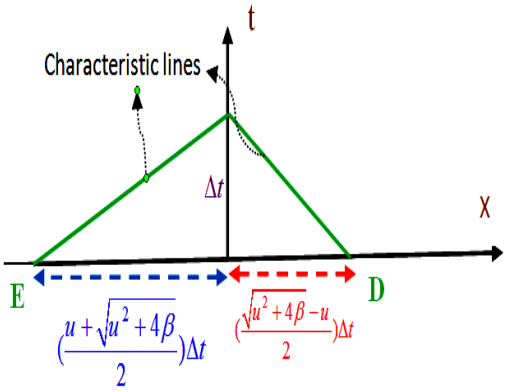

Fig. 4. Pattern for calculation of other convective fluxes.

There are two methods to obtain $p, u, and\ T$ at mentioned points. In first way, they are computed from cell center that these points stand on it, and second technique is interpolation between four cells surround these points. Here, first method has been used. In flux averaging scheme, convective fluxes are calculated as $\lambda^*=(\lambda_{i,j}+\lambda_{i+1,j})/2,\ \lambda=p, u, v$ and T.

The viscous fluxes demand the computation of derivatives at cell faces. For this purpose, Eq. (20) on the secondary cell of Fig. 5 is used. The values of u, v and T in points "A" and "B" are found by averaging from the neighboring cells.

$$\left.\frac{\partial\eta}{\partial x}\right|_{AB}=\frac{1}{S}\iint_S\frac{\partial\eta}{\partial x}ds=\frac{1}{S}\oint\eta dy=\frac{1}{S}\sum_{k=1}^{4}\eta\Delta y_k\,,\qquad(20)$$
$$\eta=u,v,T\,.$$

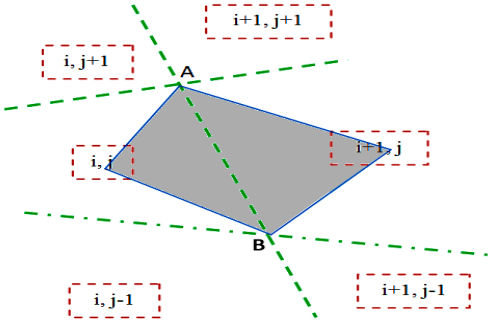

Fig. 5. Stencil for discretization of viscous fluxes.

For time discretization, fifth-order Runge-Kutta is utilized as following

$$\mathbf{Q}_{ijk}{}^{(p)}=\mathbf{Q}_{ijk}{}^{(n)}-F(\mathbf{Q}_{ijk}{}^{(p-1)}),$$
$$\alpha_p=\frac{1}{4},\frac{1}{6},\frac{3}{8},\frac{1}{2},1,\quad p=1,2,\ldots,5.\qquad(21)$$

The viscous dissipation term is neglected in energy equation for comparison purpose. At the walls, no-slip condition is applied, and pressure is extrapolated from interior domain. At the inlet, velocities and temperatures are given and pressures

are extrapolated. At the outlet, pressure is known and velocities and temperatures are extrapolated. Both plates have constant temperatures, and are stationary. For flow in cavity up and down walls are at constant temperatures and left and right walls are adiabatic. The friction factor and Nusselt number are computed by the following relations.

$$f = \frac{\frac{\partial u}{\partial y}}{\frac{1}{2}\mathrm{Re}}, \quad T_{mean} = \frac{1}{A u_{mean}} \iint T\, u\, dA,$$

$$Nu = \frac{\frac{\partial T}{\partial y}}{T_{wall} - T_{mean}} \rightarrow f_i = \frac{2\left(u_{i,2} - u_{i,1}\right)}{\Delta y\ \mathrm{Re}},$$

$$T_{mean} = \frac{1}{(wide)(u_{mean})} \sum_{j=1}^{JM} T_{\mathrm{Im},Jm}\, u_{\mathrm{Im},Jm} \Delta y,$$

$$Nu_i = \frac{\left(T_{i,2} - T_{i,1}\right)}{\Delta y\ (T_{wall} - T_{mean})},$$

$$Nu = \frac{\partial T}{\partial y} \rightarrow Nu_i = \frac{\left(T_{i,2} - T_{i,1}\right)}{\Delta y} \ (cavity\ flow).$$

5. NUMERICAL RESULTS AND DISCUSSION

To show the scheme performance, two bench marks are simulated with first-order MC and second-order flux averaging schemes. Benchmark flows were solved for a wide range of parameters (10<Re<5000, 0<Gr<1E6, 0.7<Pr<70). The friction coefficient variation versus length at different Reynolds numbers is shown in Fig. 6. The developing length is increased by growing Reynolds number. The exit velocity is compared to the analytical solution in Fig. 7. In Table 1, exit Nusselt number is shown at outlet by two mentioned methods, and error is estimated by comparing them with the analytical solution. In fully developed flow between parallel plates by exact solution the Nusselt number is 7.56.

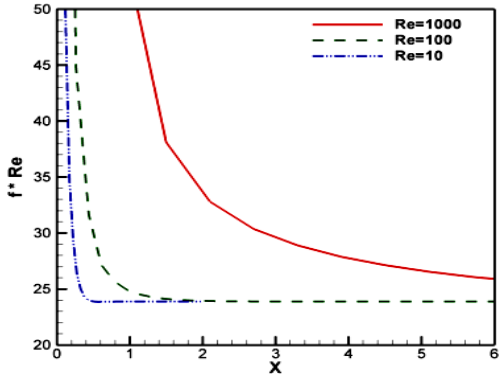

Fig. 6. f * Re variations versus length at different Reynolds numbers.

Nusselt number distribution for different Reynolds and Prandtl numbers are shown in Figs. 8 and 9. Developing heat length is increased by growing Reynolds and Prandtl numbers.

Comparisons of convergence histories for flow between parallel plates and in cavity, for two mentioned schemes, are displayed in Figs. 10 and 11. In both cases faster convergence for MC scheme has been achieved.

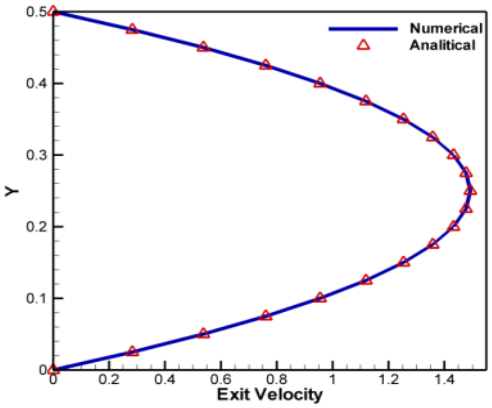

Fig. 7. Verification of exit velocity profile with analytical solution at Re=100.

Table 1 Evaluation of exit Nusselt numbers

	Length	Grid size	Schemes	Nu	Error (%)
Re=10	1.0	40*80	Ave	7.78425	2.97
			MC	7.76694	2.74
		40*40	Ave	7.89848	4.75
			MC	7.87175	4.40
Re=100	7.0	40*20	Ave	7.5553	0.20
			MC	7.57391	0.45
		100*20	Ave	7.5592	0.25
			MC	7.56039	0.27
Re=1000	60.0	100*20	Ave	7.47375	0.88
			MC	7.47859	0.81
		200*20	Ave	7.52242	0.23
			MC	7.52652	0.18

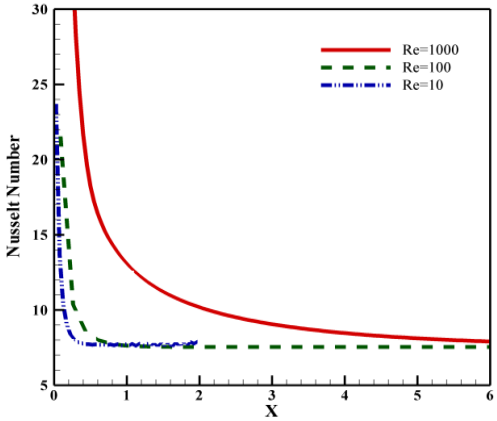

Fig. 8. Comparison of Nusselt number distributions for different Re at Pr=0.71.

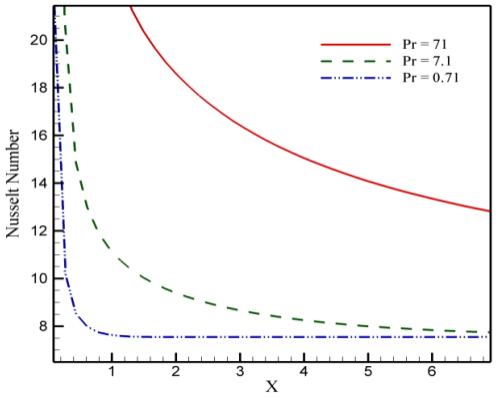

Fig. 9. Comparison of Nusselt number distributions for different Pr at Re=100.

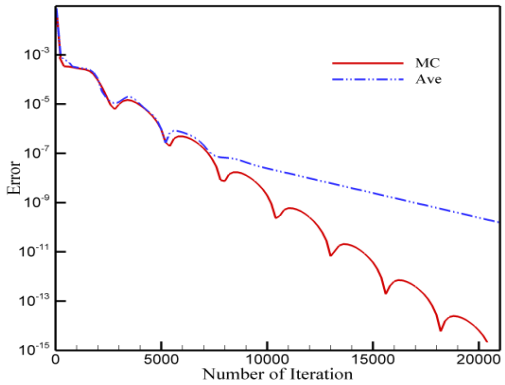

Fig. 10. Comparison of convergence histories for flow between parallel plates (Re=100, Pr=0.71).

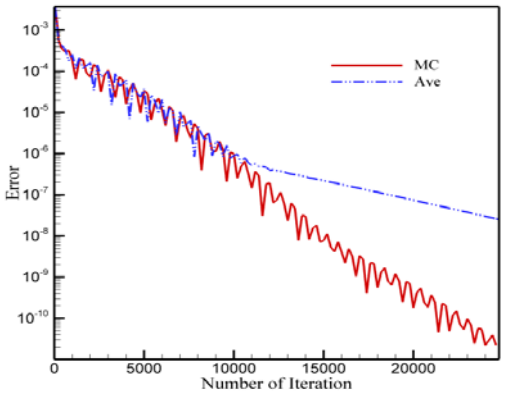

Fig. 11. Comparison of convergence histories for the cavity flow (Re=3162, Gr=1E6, Pr=0.71.

Stream lines and isotherms at Gr=0, Gr=1E6 and Pr=0.71 at different Reynolds numbers are shown and compared with that of Cheng and Liu [20] in Figs. 12-14, where good agreement is seen. Their results were obtained by fourth-order accurate compact form with 128*128 grids. In forced convection (Gr=0), by increasing Reynolds the secondary vortex that appears in the left and right bottom of cavity is being amplified and then another secondary vortex appears in the upper left.

The Richardson number, $Ri = \dfrac{Gr}{\mathrm{Re}^2}$ provides a measure for the relative importance of the thermal natural convection to the lid-driven forced convection effect. At high Grashof numbers the free convection appears and becomes important. To vary Richardson number, Grashof number is fixed at 1E6 while changing Reynolds number as Re = 316, 1000, and 3162. This variation yields Ri = 10, 1, and 0.1 which covers the natural convection dominated to forced convection dominated regimes. For Ri >1, the stable temperature gradient slowdowns the fluid movements in the middle and bottom regions of the cavity, which leads to a vertical stratification of temperature distribution in these sections. Therefore, the heat transfer is mostly through conduction in these areas and convection is active in the upper part of the cavity. When Ri < 1, the effect of mechanically-driven top lid dominates the whole cavity and produces a primary vortex with four smaller secondary vortices. To clarify, the details are shown in Figs. 15-22. In these figures, velocities, temperatures, and local Nusselt numbers are displayed. Profiles of horizontal velocity along the vertical center lines and vertical velocity along the horizontal center lines for different Re, Gr numbers are shown in Figs. 15- 18. When Reynolds number increases, the velocity extermums become larger. By Grashof number growing, the free convection becomes more significant. It changes stream lines and vortex patterns. Temperature distributions along the vertical center line for different Grashof, Prandtl, and Reynolds numbers are demonstrated in Figs. 19 and 20. At high Grashof numbers, temperature variations are more uniform than the lower one. At low Grashof numbers, temperature gradient is steep on top and bottom than the center part of cavity.

By Prandtl number growing, thermal boundary layer thickness becomes thinner and as a result temperature gradient gets sharper. The top and bottom Nusselt number distributions for different Reynolds, Grashof numbers are displayed in Figs. 21 and 22. Nusselt number on top wall is larger than the one at down wall. This is because of steep temperature gradient at the top of cavity. The heat transfer rate of the top wall generally goes down in the trend of the lid motion due to the creation and development of thermal boundary layer over the surface. On the bottom wall, however, the variation of the local heat transfer rate is more complex, and demonstrates local extermum because of the act of the primary and secondary vortices, especially for the forced convection conquered flow. The results obtained by MC and Averaging are compared with that of Iwatsu *et al*. [21] through Figs 15-22. They solved the governing equations by resorting to a well-established finite difference numerical procedure. Amended version of the MAC method was applied. Results were obtained with 256*256 grids. Good agreement for all test cases is observed and the results confirm the superiority of MC scheme in terms of convergence and accuracy. Results of Figs. 12-22 have been obtained with 128*128 grids. Grid independence is displayed in Figs. 23 and 24 for two benchmarks

Cheng [20]	MC	Flux averaging
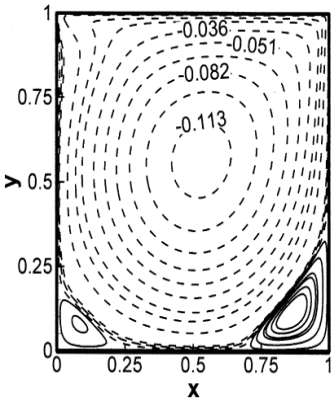	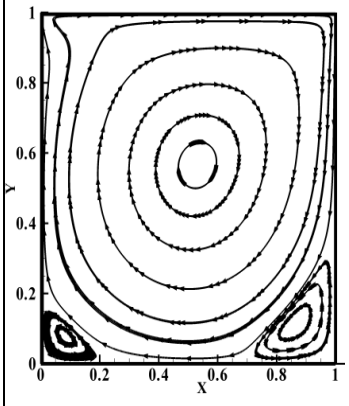	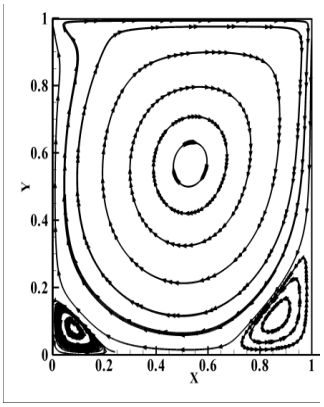
Re=1000		
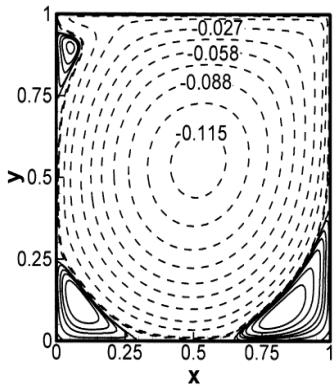	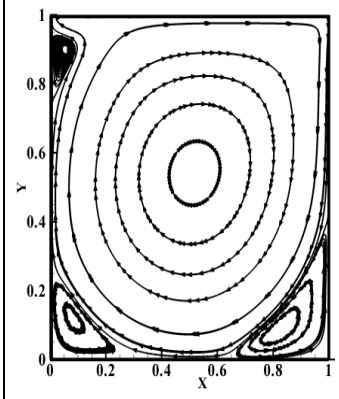	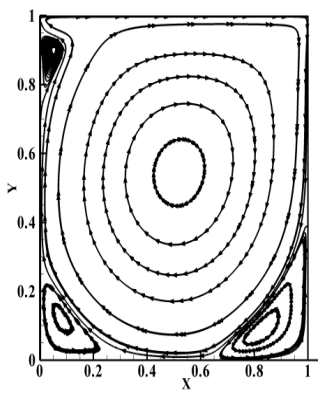
Re=3200		
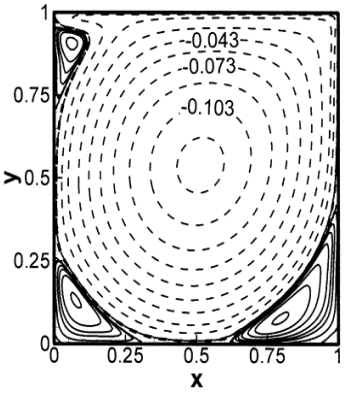	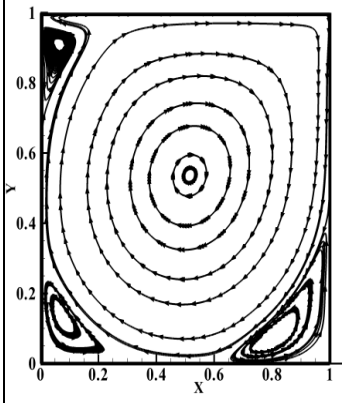	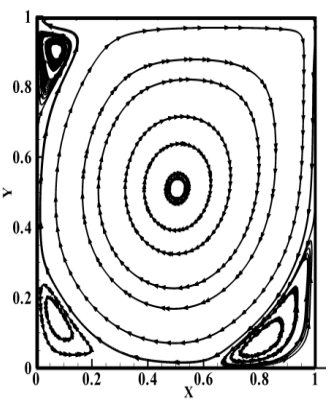
Re=5000		

Fig. 12. Comparisons of stream lines at different Re, Gr=0.

Cheng [20]	MC	Flux averaging
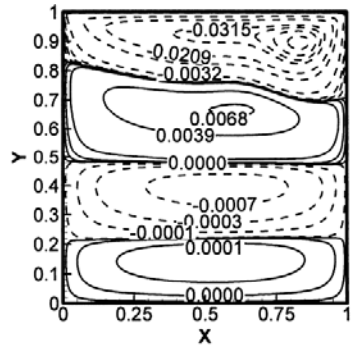	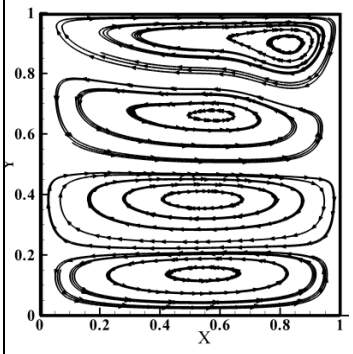	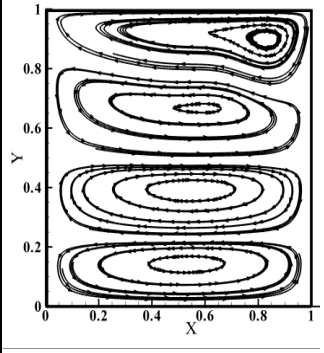
Re=316		
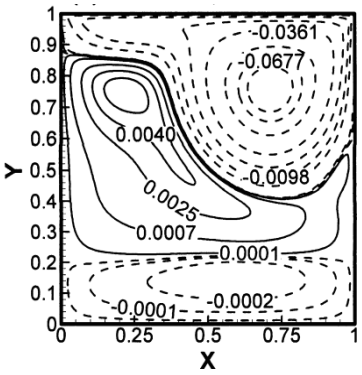	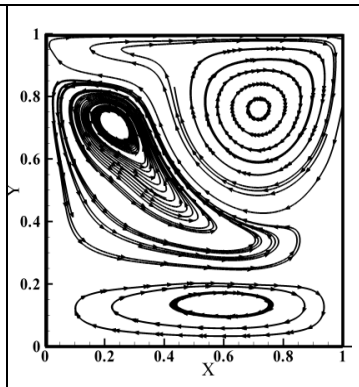	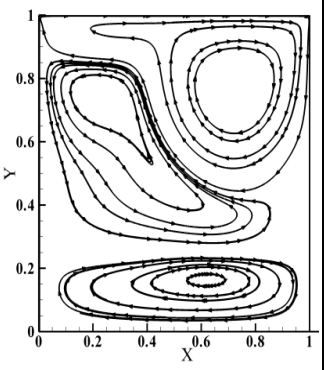
Re=1000		
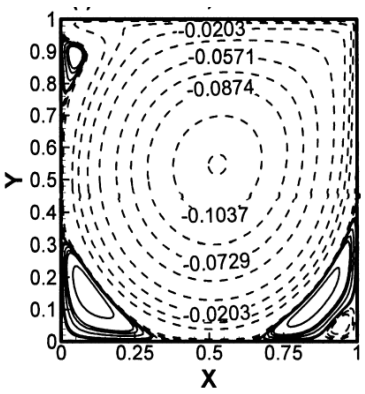	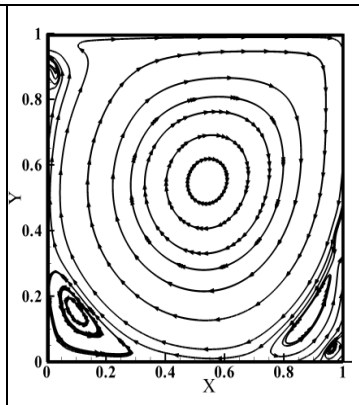	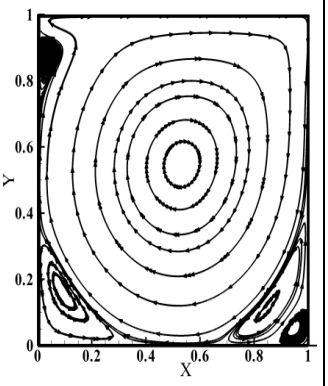
Re=3162		

Fig. 13. Comparisons of stream lines at different Re, Gr=1E6, Pr=0.71.

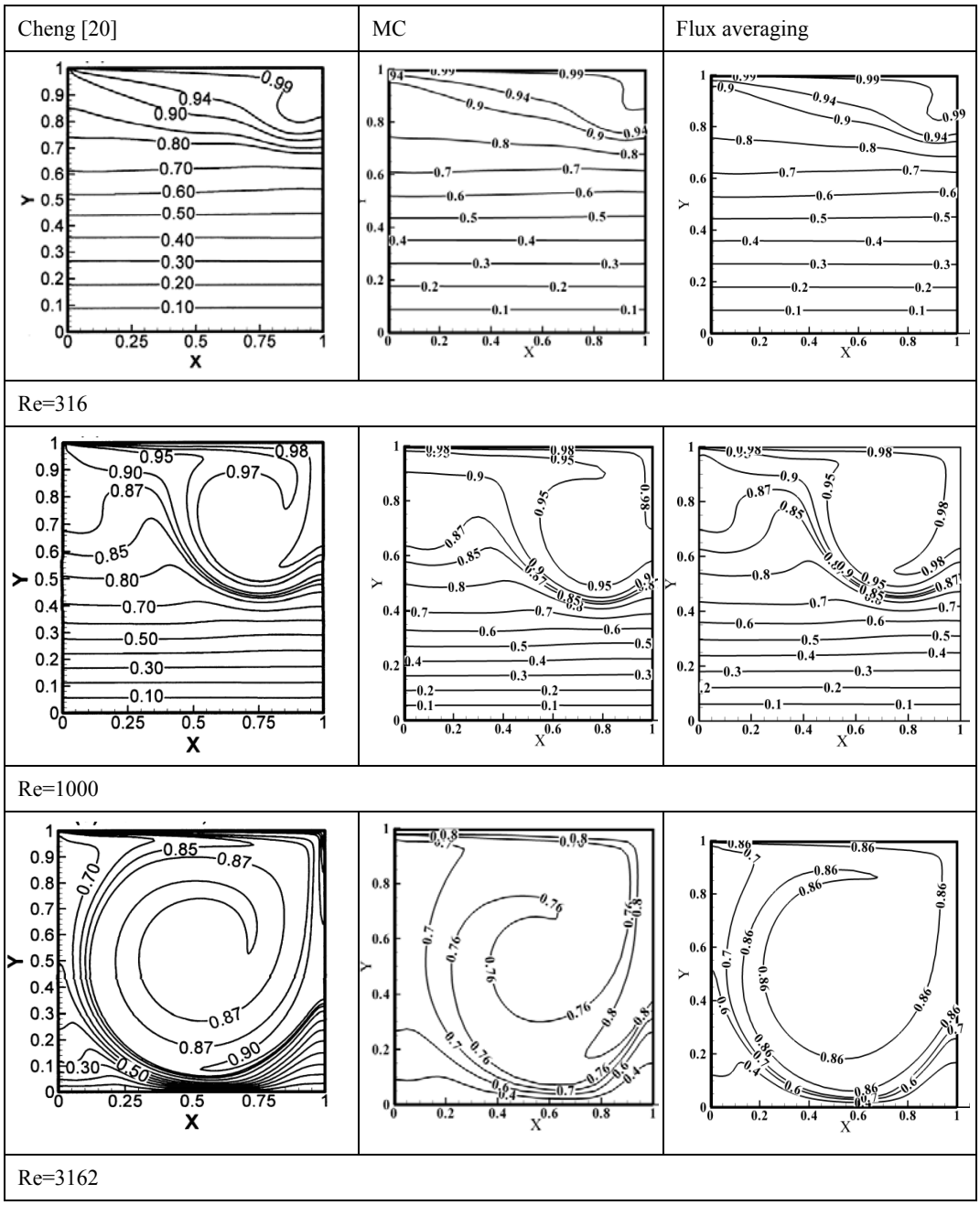

Fig. 14. Comparisons of isotherms at different Re, Gr=1E6, Pr=0.71.

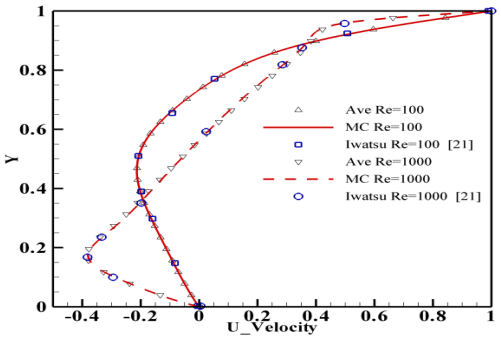

Fig. 15. Comparison of profiles for horizontal velocity along the vertical center lines at Gr=100, Pr=0.71.

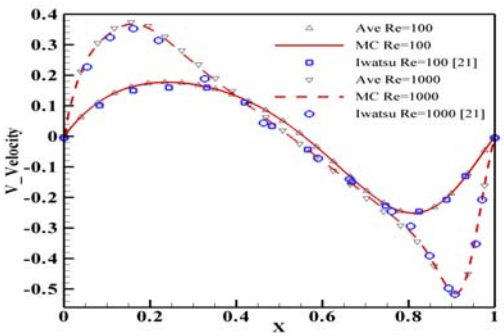

Fig. 16. Comparison of profiles for vertical velocity along the horizontal center lines at Gr=100, Pr=0.71.

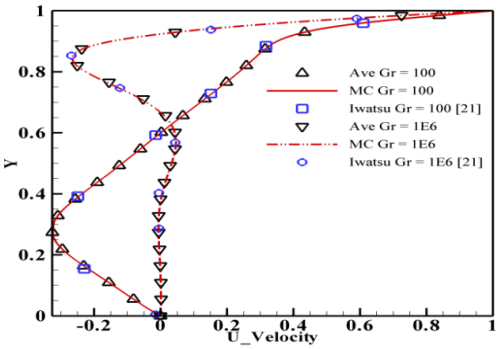

Fig. 17. Comparison of profiles for horizontal velocity along the vertical center lines at Re=400, Pr=0.71.

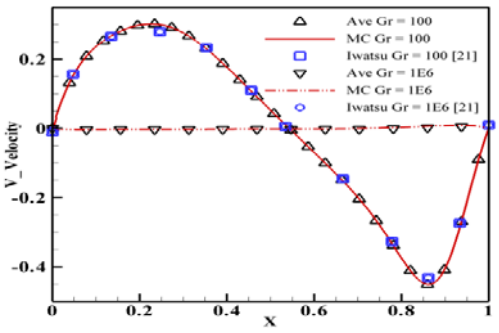

Fig. 18. Comparison of profiles for vertical velocity along the horizontal center lines at Re=400, Pr=0.71.

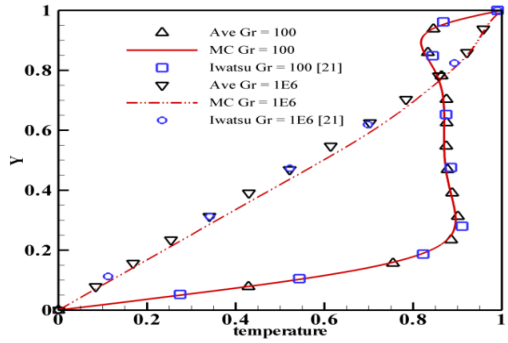

Fig. 19. Comparison of temperature distributions along the vertical center line at Re=400, Pr=0.71.

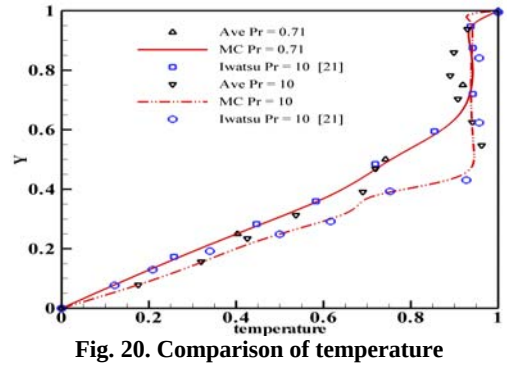

Fig. 20. Comparison of temperature distributions along the vertical center line at Re=1000, Gr=1E6.

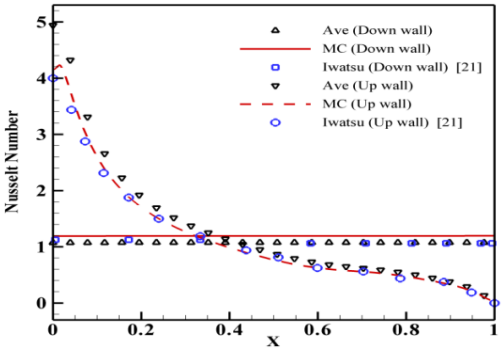

Fig. 21. Nusselt number distributions on the up and down wall (Re=400, Pr=0.71, and Gr=1E6).

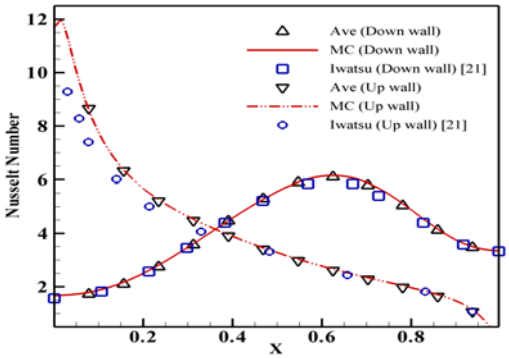

Fig. 22. Nusselt number distributions on the up and down wall (Re=400, Pr=0.71, and Gr=100).

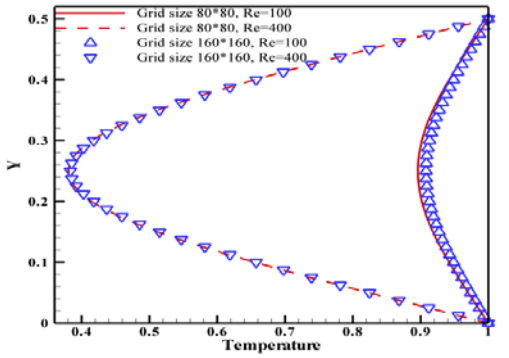

Fig. 23. Evaluation of grid independent of flow between parallel plates (Pr=0.71).

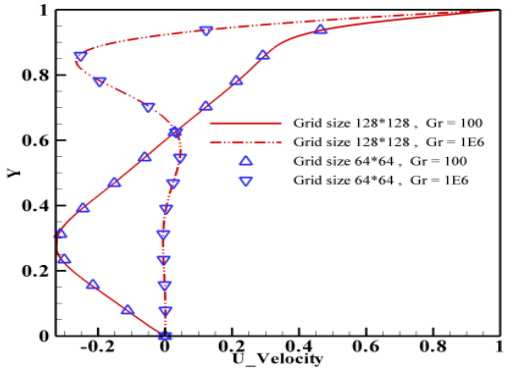

Fig. 24. Evaluation of grid independent of cavity flow (Re=400 and Pr=0.71).

5. CONCLUSION

A new scheme for solving incompressible Navier-Stokes and energy equations is presented. The convective fluxes are modeled by flux averaging and multidimensional characteristic (MC) methods. First-order MC and second-order averaging schemes are utilized to simulate flow between parallel plates and in a cavity, for a wide range of Reynolds, Grashof, and Prandtl numbers. The new scheme benefits multidimensional characteristics, which have been derived for the first time for incompressible thermo-flow equations with artificial compressibility within the finite-volume framework to evaluate convective fluxes. Since MC applies characteristic compatibility equations, it presents stable solutions and without any artificial dissipation even at higher Reynolds numbers. Good agreement for all the test cases is observed, and results confirm the superiority of MC scheme in terms of convergence and accuracy.

REFERENCES

Rahmati, A. R., M. Ashrafizaadeh and E. Shirani (2014). A Multi-Relaxation-Time Lattice Boltzmann Method on Non- Uniform Grids for Large Eddy Simulation of Rayleigh-Bénard Convection Using Two Sub-Grid Scale Models. *Journal of Applied Fluid Mechanics* 8: 123-132.

Billah, M. M., M. M. Rahman, U. M. Sharif, N. A. Rahim, R. Saidur and M. Hasanuzzaman (2011). Numerical analysis of fluid flow due to mixed convection in a lid-driven cavity having a heated circular hollow cylinder. *International Communications in Heat and Mass Transfer* 38(8), 1093-1103.

Chorin, A. J. (1997). A Numerical Method for Solving Incompressible Viscous Flow Problems. *Journal of Computational Physics* 135(2), 118-125.

Santos, E. D., G. L. Piccoli, F. H. R. França and A. P. Petry (2011). Analysis of mixed convection in transient laminar and turbulent flows in driven cavities. *International Journal of Heat and Mass Transfer* 54(21–22), 4585-4595.

Drikakis, D., P. A. Govatsos and D. E. Papantonis (1994). A characteristic-based method for incompressible flows. *International Journal for Numerical Methods in Fluids* 19, 667-685.

Ghasemi, J. and S. E. Razavi (2010). On the finite-volume Lattice Boltzmann modeling of thermo-hydrodynamics. *Computers and Mathematics with Applications* 60(5), 1135-1144.

Haeri, S. and J. S. Shrimpton (2013). A new implicit fictitious domain method for the simulation of flow in complex geometries with heat transfer. *Journal of Computational Physics* 237(0), 21-45.

Ohwada, T., P. Asinari and D. Yabusaki (2011). Artificial compressibility method and lattice Boltzmann method: Similarities and differences. *Computers & Mathematics with Applications* 61(12), 3461-3474.

Raji, A., M. Hasnaoui, M. Naïmi, K. Slimani and M. T. Ouazzani (2012). Effect of the subdivision of an obstacle on the natural convection heat transfer in a square cavity. *Computers and Fluids* 68(0), 1-15.

Rehena, N. and A. Alim (2014). ,Finite Element Simulation of Forced Convection in a Flat Plate Solar Collector: Influence of Nanofluid with Double Nanoparticles. *Journal of Applied Fluid Mechanics* 7, 543-556.

Selimefendigil, F. and H. F. Öztop (2014). Numerical investigation and dynamical analysis of mixed convection in a vented cavity with pulsating flow. *Computers and Fluids* 91(0), 57-67.

Shakir, A. M., A. K. Mohammed and M. I. Hasan (2011). Numerical investigation of counter flow microchannel heat exchanger with slip flow heat transfer. *International Journal of Thermal Sciences* 50(11), 2132-2140.

Sivasankaran, S., V. Sivakumar and A. K. Hussein (2013). Numerical study on mixed convection in an inclined lid-driven cavity with discrete heating. *International Communications in Heat and Mass Transfer* 46(0), 112-125.

Srinivasa, A. H. and A. T. Eswara (2013). Unsteady free convection flow and heat transfer from an isothermal truncated cone with variable viscosity. *International Journal of Heat and Mass Transfer* 57(1): 411-420.

Tamamidis, P., G. Zhang and D. N. Assanis (1996). "Comparison of Pressure-Based and Artificial Compressibility Methods for Solving 3D Steady Incompressible Viscous Flows. *Journal of Computational Physics* 124(1), 1-13.

Tmartnhad, I., M. El Alami, M. Najam and A. Oubarra (2008). Numerical investigation on mixed convection flow in a trapezoidal cavity heated from below. *Energy Conversion and Management* 49(11), 3205-3210.